

Supplementary Information for

**Cascaded energy landscape as a key driver for slow yet efficient charge separation
with small energy offset in organic solar cells**

Shin-ichiro Natsuda¹, Toshiharu Saito¹, Rei Shirouchi¹, Yuji Sakamoto¹, Taiki Takeyama¹, Yasunari Tamai^{1,2},
Hideo Ohkita¹*

¹ Department of Polymer Chemistry, Graduate School of Engineering, Kyoto University, Katsura, Nishikyo,
Kyoto 615-8510, Japan

² Japan Science and Technology Agency (JST), PRESTO, 4-1-8 Honcho Kawaguchi, Saitama 332-0012, Japan

* to whom correspondence: tamai@photo.polym.kyoto-u.ac.jp

Table of Contents

Experimental details

Absorption and PL spectra of pristine PM6 and Y6 films

EQE and EL spectra of the optimized PM6/Y6 blend

Absorption spectra of PTB7-Th/Y6 and P3HT/Y6 blend films

Absorption spectrum of the D-rich PM6/Y6 blend film

PL quenching

Marcus fitting

Cyclic voltammetry

Photoelectron yield spectroscopy

Device performance

Device performance of other blends

Assignments of the TA spectra

Time evolution of the TA spectra of the PTB7-Th/Y6 blend film

Excitation fluence dependence of exciton decay kinetics

Charge generation kinetics in the PM6/Y6 blend

TA spectra of the PM6/Y6 blend film after band-edge excitation

Reorganization energy

Late emergence of the 760 nm signal in the PM6/Y6 blend film

Supplementary comment on the Y6 GSB peak shift

Time evolution of EA

Normalized time evolution of EA

Difference in the time evolution of charge TA and EA signals

TA spectra of the PM6/Y6 blend film after polymer selective excitation

Excitation fluence dependence of charge decay kinetics

Temperature dependence of the PM6/Y6 blend

Triplet generation via bimolecular charge recombination

TA data processing via total variation regularization

Experimental details

Film preparation

Films for all spectroscopic measurements were prepared on quartz substrates, which were sequentially cleaned by sonication in toluene, acetone, and ethanol for 15 min each. The optimized PM6/Y6 and PTB7-Th/Y6 blends (1:1.2 w/w, total concentration of 17.6 mg mL^{-1}) were dissolved in chloroform with 0.5 vol% chloronaphthalene as an additive and left to stir at room temperature overnight. Thin films were spin-coated onto the cleaned substrates in a N_2 -filled glovebox and then thermally annealed at 110°C for 5 min. Similarly, the P3HT/Y6 blend (1:1.2 w/w, total concentration of 17.6 mg mL^{-1}) was dissolved in chloroform, but without any additives. It was also stirred at room temperature overnight and spin-coated in the glovebox and then thermally annealed at 140°C for 10 min. The D-rich PM6/Y6 blend was prepared by the same method as the optimized PM6/Y6 blend, but with a D/A blend ratio of 95:5 (w/w, total concentration of 40 mg mL^{-1}). For TA measurements, the samples were encapsulated in the glovebox.

Device fabrication

Photovoltaic devices were fabricated on ITO/glass substrates (Geomatec Co., 1006, $10 \Omega \text{ sq.}^{-1}$), which were sequentially cleaned by sonication in toluene, acetone, and ethanol for 15 min each, followed by UV- O_3 treatment (Nippon Laser and Electronics Lab.) for 30 min. PEDOT:PSS (Clevios, Al4083) was spin-coated onto the substrates ($\sim 30 \text{ nm}$) and dried on a hot plate (150°C , 20 min) under ambient conditions. Thereafter, the aforementioned active layers were spin-coated in the glovebox under the same conditions. Subsequently, PDINO was spin-coated from a methanol solution (2 mg mL^{-1}), and $\sim 80 \text{ nm}$ of Al was thermally evaporated onto the PDINO layer. The devices were placed in a N_2 -filled chamber for $J-V$, EQE and EL measurements.

Steady-state absorption and emission spectra

UV-visible absorption spectra were acquired using a UV-visible spectrometer (Hitachi, U-4100). The PL spectra were measured using a fluorescence spectrophotometer (Horiba Jobin Yvon, NanoLog) equipped with a photomultiplier tube (Hamamatsu, R928P) and a liquid- N_2 -cooled InGaAs near-IR array detector (Horiba Jobin Yvon, Symphony II). The excitation wavelength was set to 790 nm. The EL spectra were measured using the same setup with a DC voltage and current source/monitor (Advantest, R-6243).

***J-V* and EQE measurements**

The *J-V* characteristics were measured using a DC voltage and current source/monitor (Keithley, 2611B) in the dark and under AM1.5G simulated solar illumination at 100 mW cm⁻². The light intensity was corrected using a calibrated Si photodiode (Bunko-Keiki, BS-520). The EQE spectra were measured using a spectral response measurement system (Bunko-Keiki, ECT-25D).

CV

Materials were dissolved in acetonitrile/*o*-dichlorobenzene (9:1 v/v) solutions with 0.1 M tetrabutylammonium perchlorate as the supporting electrolyte. CV measurements were performed using a potentiostat (Princeton Applied Research, Potentiostat/Galvanostat Model 273A) at a scanning rate of 5 mV s⁻¹. A Pt mesh, a Ag/AgCl wire, and a thinly sliced ITO substrate were used as the counter, reference, and working electrode, respectively. Ferrocene was used as an internal reference. The HOMO energies were then evaluated from the onset potential of the first oxidation peak φ_{OX} as $E_{\text{HOMO}} = -(\varphi_{\text{OX}} + 4.8 - \varphi_{\text{Fe/Fe}^+})$, where $\varphi_{\text{Fe/Fe}^+}$ is the redox potential of ferrocene/ferrocenium.

PYS

The IEs were measured using a photoelectron yield spectrometer (Riken Keiki, AC-3) with a power setting of 5 nW. Calibration was performed using an Au layer. All films were prepared on ITO/glass substrates. The threshold energy for the photoelectron emission was evaluated on the basis of the cubic root of the photoelectron yield plotted against the incident photon energy.

TRPL measurements

The TRPL spectra and PL decay kinetics were measured by the time-correlated single-photon-counting (TCSPC) method (Unisoku Scientific Instruments, LSP-200T-VN-EM) with an excitation wavelength of 660 nm. The full width at half maximum of the instrument response function (IRF) is 160 ps. Decay time constant was analyzed by deconvoluting the observed decay with the IRF and an exponential function with a constant fraction.

TA measurements

Femtosecond TA data were collected using a pump and probe femtosecond TA spectroscopy system, which consisted of a TA spectrometer (Ultrafast Systems, Helios) and a regenerative amplified Ti:sapphire laser

(Spectra-Physics, Hurricane). A fundamental pulse with a wavelength of 800 nm was used as the excitation source for Y6, whereas it was converted with an ultrafast optical parametric amplifier (Spectra-Physics, TOPAS) for excitation wavelength dependence measurements. The TA data were collected over a time range from -5 ps to 3 ns. The temperature dependence was measured using a liquid-N₂-cooled cryostat (Oxford Instruments, Optistat DN-V).

The microsecond TA data were collected using a sensitive microsecond TA system. A Nd:YAG laser (Elforlight, SPOT-10-200-532) operating at a wavelength of 532 nm was used as the excitation source. White light from a tungsten lamp with a stabilized power source was used as the probe light. Two monochromators and appropriate optical cut-off filters were placed before and after the sample to increase the signal-to-noise ratio (SNR). Further details of our TA setup have been presented elsewhere.^{S1}

TA data processing

TA data were denoised by total variation (TV) regularization method to increase SNR. Details of this method are described in the “TA data processing via total variation regularization” section.

DFT calculations

DFT calculations were performed for model compounds of isolated PM6 dimer and Y6, wherein alkyl side chains were shortened to reduce the computational effort, using the Gaussian 16 rev. A package.^{S2} In order to obtain the reorganization energy, these molecules were first optimized in the ground state using the B3LYP functional and 6-311G(d,p) basis set. Second, the positively charged PM6 dimer and negatively charged Y6 were optimized using the 6-31G(d) and 6-31+G(d) basis sets, respectively. Third, time-dependent (TD)-DFT with B3LYP/6-31+G(d) was carried out to optimize Y6 in the singlet excited state. Finally, the positively charged PM6 dimer in the ground state geometry and negatively charged Y6 in the excited state geometry were calculated using the 6-31G(d) and 6-31+G(d) basis sets, respectively. The reorganization energy was then obtained from the difference of the total energy between participants.

Absorption and PL spectra of pristine PM6 and Y6 films

E_{S1} for pristine PM6 and Y6 films was determined to be 1.90 and 1.39 eV, respectively, from the intersection of the absorption and PL spectra.

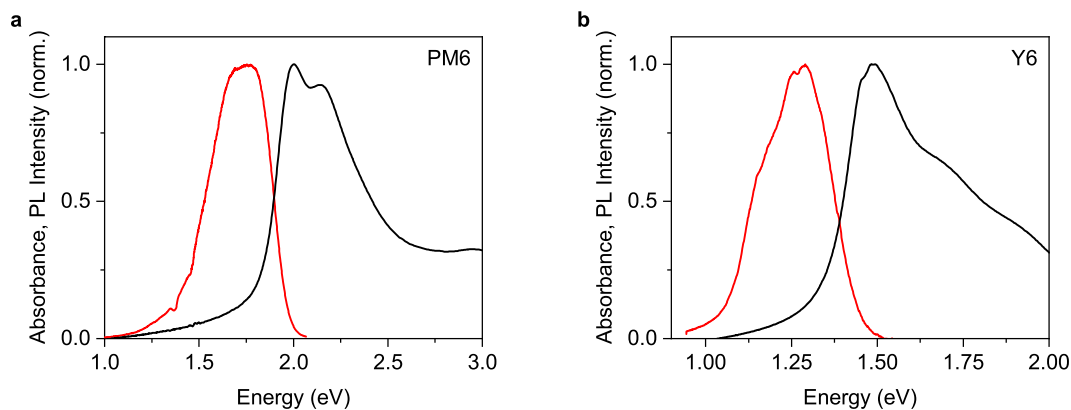


Fig. S1. Absorption (black) and PL (red) spectra of pristine (a) PM6 and (b) Y6 films.

EQE and EL spectra of the optimized PM6/Y6 blend

E_{S1} for the optimized PM6/Y6 blend was determined to be 1.41 eV from the intersection of the EQE and EL spectra.

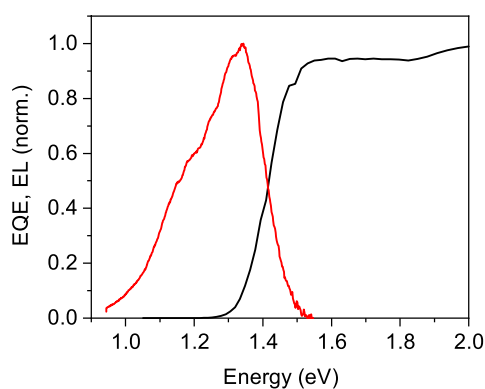


Fig. S2. EQE (black) and EL (red) spectra of the optimized PM6/Y6 blend device.

Absorption spectra of PTB7-Th/Y6 and P3HT/Y6 blend films

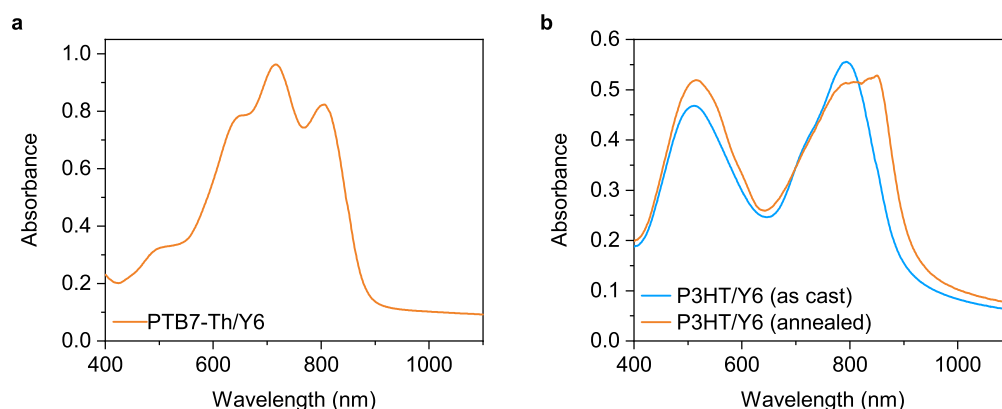


Fig. S3. **a** Absorption spectrum of the PTB7-Th/Y6 blend film. **b** Absorption spectra of the P3HT/Y6 blend film measured before and after thermal annealing at 140 °C for 10 min.

Absorption spectrum of the D-rich PM6/Y6 blend film

The red line in Fig. S4 shows the absorption spectrum of the D-rich PM6/Y6 blend film (95:5 w/w). The peak wavelength corresponding to Y6 absorption in the D-rich blend was clearly blueshifted relative to that of the optimized PM6/Y6 blend film (1:1.2 w/w), indicating that Y6 is more disordered in the D-rich film than that in the optimized blend.

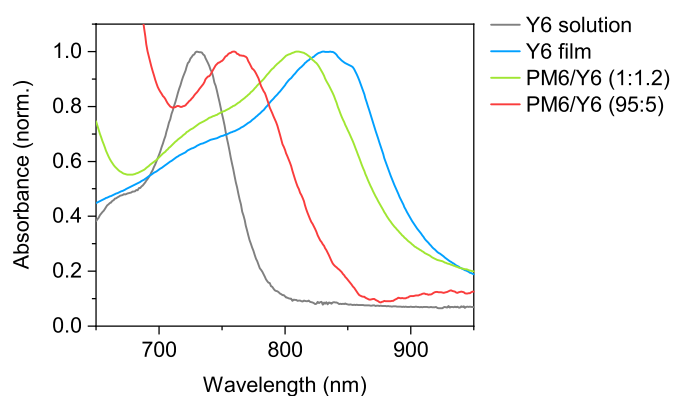


Fig. S4. Absorption spectrum of the D-rich PM6/Y6 blend film (red). Absorption spectra of the optimized PM6/Y6 blend (1:1.2 w/w, green) as well as pristine Y6 in the solution (grey) and solid states (blue) are also shown as references.

PL quenching

The PL quenching yield was defined as the PL intensity ratio, which was ~97%, >99%, and >99% for the PM6/Y6, PTB7-Th/Y6, and P3HT/Y6 blend films, respectively (Fig. S5), indicating that almost all Y6 excitons generated in these blend films dissociate into charges. Previous studies have revealed that Y6 forms crystalline domains as large as 20–30 nm in the PM6/Y6 blends.^{S3-S5} Such large domains sometimes result in inefficient charge generation because some excitons cannot reach the D/A interface; however, the PL quenching efficiency of ~97% indicates that almost all Y6 excitons can reach the interface and undergo hole transfer. We previously determined the diffusion constant for Y6 singlet excitons to be $2.1 \times 10^{-2} \text{ cm}^2 \text{ s}^{-1}$,^{S6} which corresponds to a mean free path L_D , defined as $L_D = (6D\tau)^{0.5}$, where D is the diffusion constant of Y6 excitons and τ is the exciton lifetime in the blend film (~6.0 ps), of Y6 singlet excitons in the blend film of ~8.7 nm. This indicates that even the excitons generated at the center of the Y6 domain can reach the D/A interface owing to the fast exciton diffusion. On the other hand, the high PL quenching efficiency also implies that almost all charges in the PM6/Y6 blend film decay nonradiatively to the ground state. Recently, Gillett et al. reported that ~90% of the charges decay through the formation of non-emissive Y6 triplet excited states.^{S7} Therefore, there is still considerable room to further reduce the voltage loss incurred by nonradiative charge recombination.

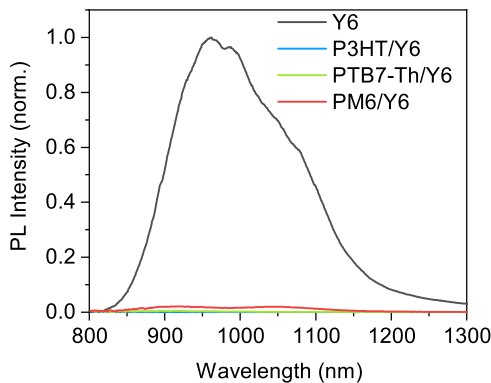


Fig. S5. PL spectra of PM6/Y6 (red), PTB7-Th/Y6 (green), and P3HT/Y6 (blue) blend films, as well as that of a pristine Y6 film (black). The PL intensities were corrected for differences in absorbance at the excitation wavelength of 790 nm.

Marcus fitting

Fig. S6a shows the normalized PL spectra of the PM6/Y6 and PTB7-Th/Y6 blend films as well as that of the pristine Y6 film. Compared to the pristine Y6 film, the PM6/Y6 blend film exhibited a more pronounced PL band at ~1050 nm. Interestingly, this band was not observed for the PTB7-Th/Y6 blend film, indicating that the attribution of this band to a vibronic band of Y6 fluorescence is inappropriate (although there should be some overlap of the vibronic sub-band of Y6 fluorescence as well). Fig. S7a shows the TRPL spectra of the PM6/Y6 blend film. As mentioned in the main text, the PM6/Y6 blend exhibits a longer decay component peaking at ~1050 nm. Therefore, the PL band peaking at ~1050 nm in Fig. S6a can be attributable to the CT emission; this assignment is consistent with a previous report, wherein the authors extracted the CT emission by comparing the PL and EL spectra.^{S8}

As shown in Fig. S6c, the CT emission part of the reduced PL spectrum I_{PL}/E can be fitted by a Gaussian function (Equation S1),^{S9,S10} where λ , k_B , and T are the reorganization energy, the Boltzmann constant, and absolute temperature, respectively. The parameter f is proportional to the square of the electronic coupling matrix element. From the fitting, E_{CT} was determined to be 1.29 eV. We also applied the same fitting to the TRPL spectrum and obtained E_{CT} of 1.30 eV (Fig. S7b). These values are very close to a recently reported E_{CT} of 1.27 eV determined by EA spectroscopy.^{S11}

$$\frac{I_{\text{PL/EL}}}{E} = \frac{f}{\sqrt{4\pi\lambda k_B T}} \exp \left[-\frac{(E_{\text{CT}} - \lambda - E)^2}{4\lambda k_B T} \right] \quad (\text{S1})$$

Fig. S6b shows the normalized EL spectra of the PM6/Y6 and PTB7-Th/Y6 devices as well as that of a pristine Y6 device. The PTB7-Th/Y6 device showed a clear CT emission at ~1110 nm. In contrast, a superposition of the locally-excited (LE) and CT emissions was observed in the PM6/Y6 device, indicating that E_{CT} is slightly higher in energy in the PM6/Y6 blend than in the PTB7-Th/Y6 blend. The absence of the clear CT emission peak in the EL spectrum of the PM6/Y6 device may be because the repopulation of the LE state is more efficient under a forward bias than that in the PL condition (no applied bias). Although the CT emission is less distinct than that in the PL spectrum, we also performed the same fitting on a shoulder at ~1050 nm, yielding somewhat larger E_{CT} of 1.44 eV (Fig. S6d). Because the CT emission is more distinct in the PL spectrum than in the EL spectrum, we believe that E_{CT} evaluated from the PL spectrum should be more reliable. However, since some uncertainties remain, such as the effect of overlap with the Y6 fluorescence, we use E_{CT} of 1.29 eV with a caveat that this value is an estimate only.

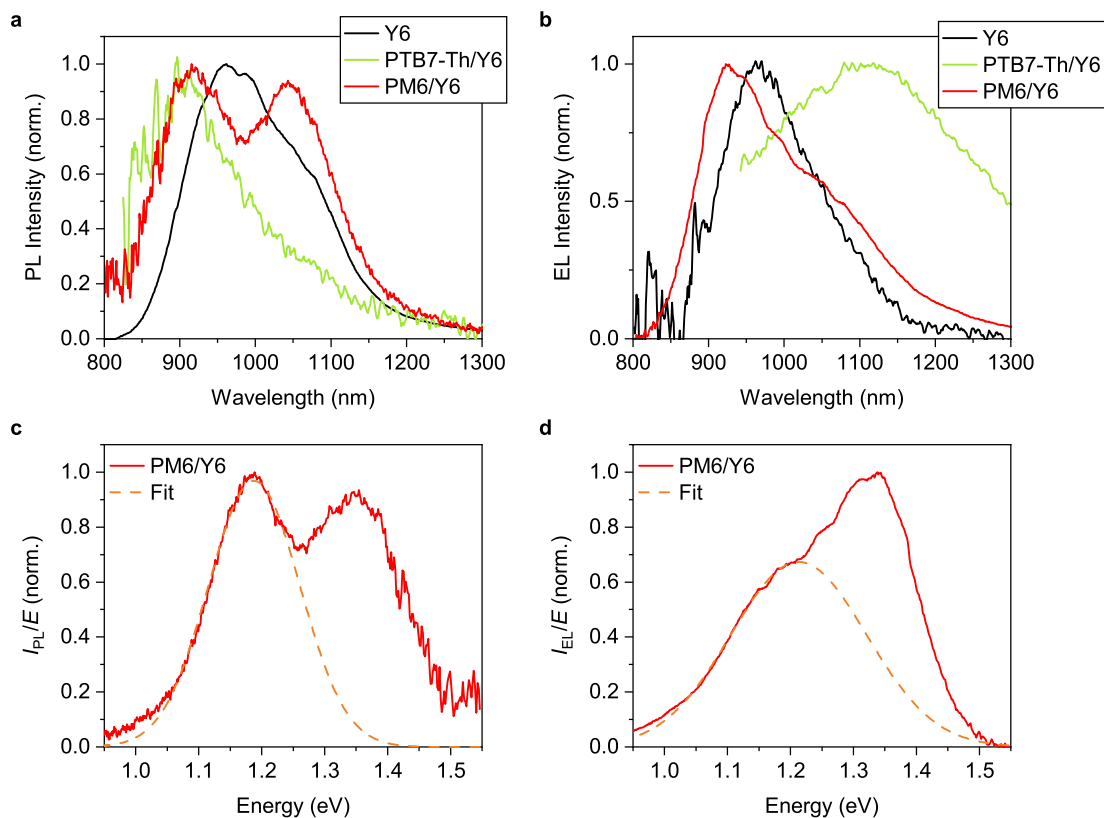


Fig. S6. **a** Normalized PL spectra. **b** Normalized EL spectra. **c** Reduced PL spectrum for the PM6/Y6 blend and **d** reduced EL spectrum for the PM6/Y6 device. Broken lines in **(c)** and **(d)** represent the best fitting curves obtained using a Gaussian function (Equation S1). Note that the emissions from the P3HT/Y6 blends were too weak to be detected.

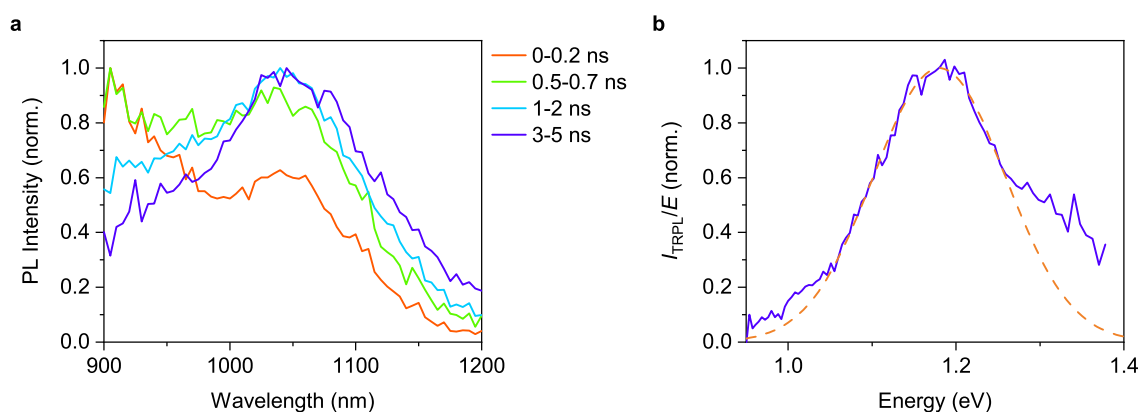


Fig. S7. **a** The TRPL spectra of the PM6/Y6 blend film. **b** Reduced TRPL spectrum for the PM6/Y6 blend (3–5 ns) The broken line represents the best fitting curve obtained using a Gaussian function (Equation S1).

Cyclic voltammetry

The HOMO energies in the solution state were evaluated using CV to be -5.23 and -5.38 eV for PM6 and Y6, respectively. These values are slightly shallower than those previously reported.^{S12} This is probably due to the difference in the scanning rate of the CV measurements because scanning too fast may overestimate the onset value. We measured cyclic voltammograms as slowly as possible (5 mV s^{-1}) to approach the reversible condition.^{S13} It should be emphasized that what is important here is the relative difference in the HOMO energies between PM6 and Y6. The HOMO energy difference was only 0.15 eV and the small HOMO offset obtained from CV is consistent with previous reports.^{S12}

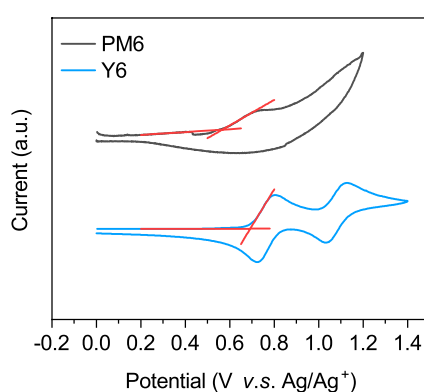


Fig. S8. Cyclic voltammograms of PM6 (black) and Y6 (blue). The HOMO energies were evaluated to be -5.23 eV (PM6) and -5.38 eV (Y6) from the onset determined from the intersection of the two tangents (red lines) for the first oxidation peak. Ferrocene was used as an internal reference.

Photoelectron yield spectroscopy

The IE in the solid state were determined using PYS to be -5.24 and -5.76 eV for PM6 and Y6, respectively, which indicates the presence of a large HOMO energy offset in the solid state. This result agrees with that of Karuthedath et al.^{S14}

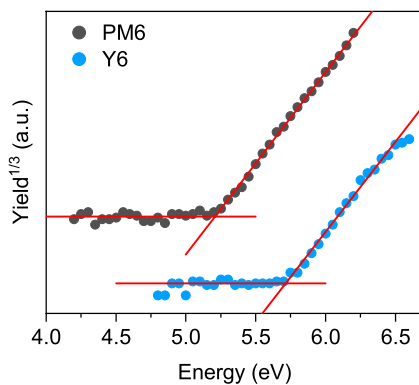


Fig. S9. Photoelectron yield spectra of pristine PM6 (black) and Y6 (blue) films.

Device performance

Fig. S10 shows the J - V characteristics and the EQE spectrum of the optimized PM6/Y6 device. Our devices reproduce the J - V characteristics in previous reports.

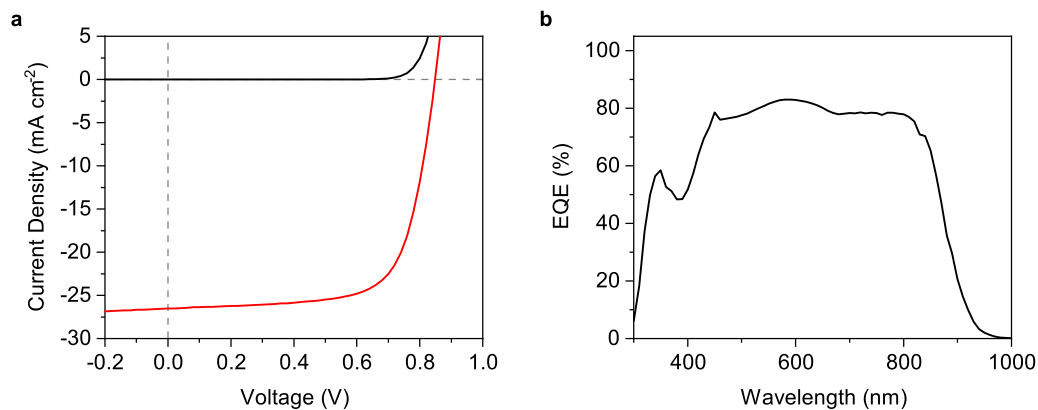


Fig. S10. **a** J - V characteristics of a PM6/Y6 device measured in the dark (black) and under simulated AM1.5G illumination (100 mA cm^{-2} , red). The device parameters are summarized in Table S1. **b** EQE spectrum of the same device.

Table S1. J - V characteristics of the PM6/Y6 device

J_{SC} (mA cm^{-2})	$J_{SC}^{\text{calc. } a}$ (mA cm^{-2})	V_{OC} (V)	FF	PCE (%)
26.5	25.0	0.848	0.703	15.8

^a J_{SC} calculated by integrating the EQE spectrum

Device performance of other blends

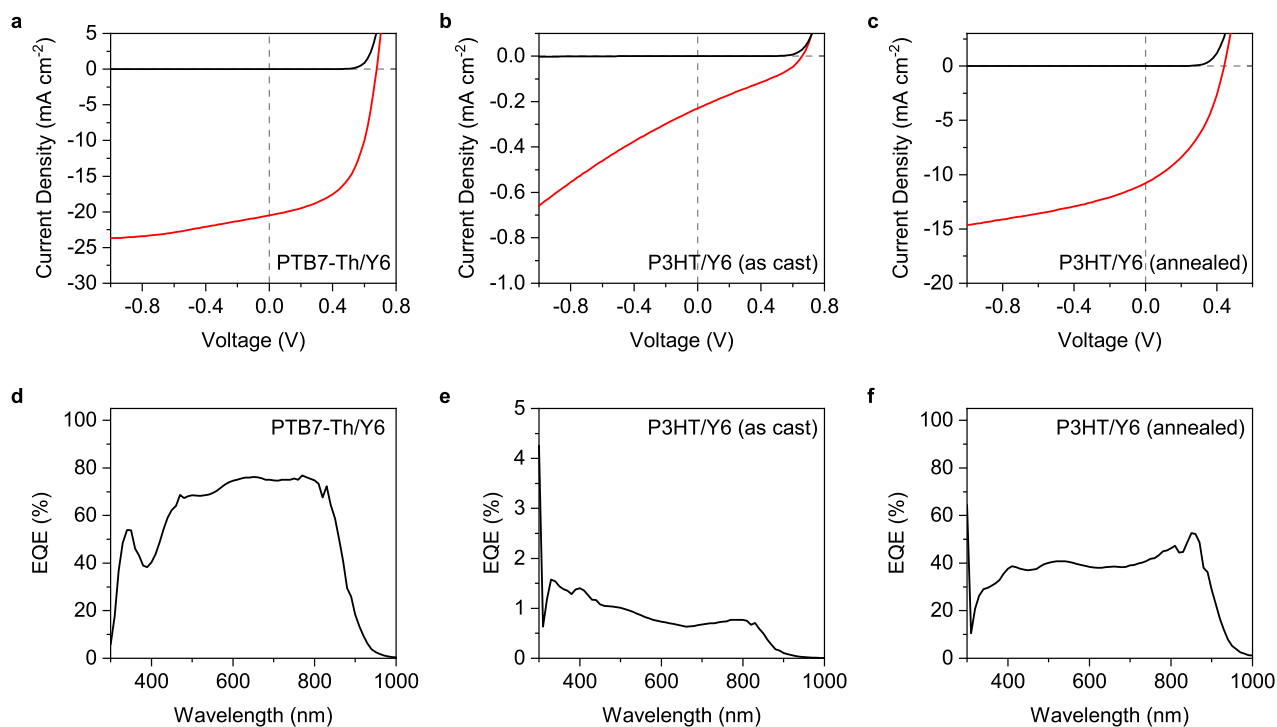


Fig. S11. J - V characteristics of (a) PTB7-Th/Y6, (b) as-cast P3HT/Y6, and (c) annealed P3HT/Y6 devices measured in the dark (black) and under simulated AM1.5G illumination (100 mA cm⁻², red). The device parameters are summarized in Table S2. EQE spectra of (d) PTB7-Th/Y6, (e) as-cast P3HT/Y6, and (f) annealed P3HT/Y6 devices.

Table S2. J - V characteristics of the PTB7-Th/Y6 and P3HT/Y6 devices

Sample	J_{SC} (mA cm ⁻²)	$J_{SC}^{calc. a}$ (mA cm ⁻²)	V_{OC} (V)	FF	PCE (%)
PTB7-Th/Y6	20.8	22.7	0.675	0.533	7.5
P3HT/Y6 (as-cast)	~0.22	~0.26	0.652	0.301	~0.04
P3HT/Y6 (annealed)	10.1	14.1	0.413	0.403	1.7

^a. J_{SC} calculated by integrating the EQE spectrum

Assignments of the TA spectra

Fig. S12 summarizes the assignments of the TA spectra. Here, we provide details of these assignments.

As we previously reported, Y6 singlet excitons exhibit a sharp PIA band at ~930 nm, a broad PIA tail above 1200 nm, and GSB at 850 nm (Fig. S13). The singlet PIA and GSB are redshifted compared with that of the PM6/Y6 blend film, as discussed in detail in the main text.

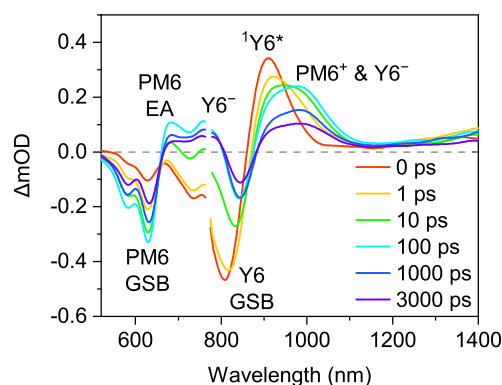


Fig. S12. Summary of assignments of the TA spectra. $^1\text{Y6}^*$: singlet excitons of Y6, Y6^- : anions of Y6, Y6 GSB: ground-state bleaching of Y6, PM6^+ : hole polarons of PM6, PM6 GSB: ground-state bleaching of PM6, and PM6 EA: transient electroabsorption of PM6.

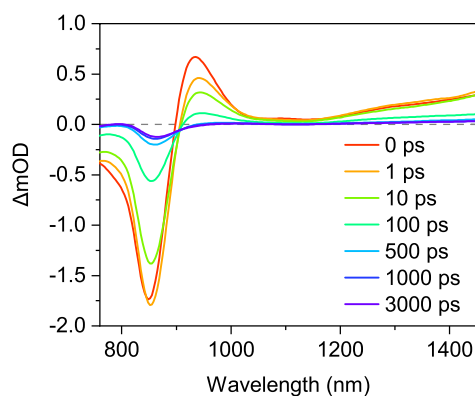


Fig. S13. TA spectra of a pristine Y6 film. The excitation wavelength was 800 nm with a fluence of $3.8 \mu\text{J cm}^{-2}$. Reprinted with permission from ref. S6. Copyright 2021 American Chemical Society.

The long-lived PIA bands in Fig. 3 are still observed on the microsecond time scale except for the positive signals at 680 nm (Fig. S14a). The absence of the 680 nm signal on microsecond time scale is consistent with our assignment of this signal to be attributable to EA due to dipole-like local electric field generated by electron-hole pairs at the interfaces because there exist no CT states on microsecond time scale. At the same

time, this finding also suggests that the 780 nm band is not attributable to EA of Y6. The existence of the positive signals at 780 nm and 960 nm on the microsecond time scale indicates that these bands can be attributable to charged species because Y6 triplet excitons exhibits a PIA band at ~ 1400 nm.^{S6,S7}

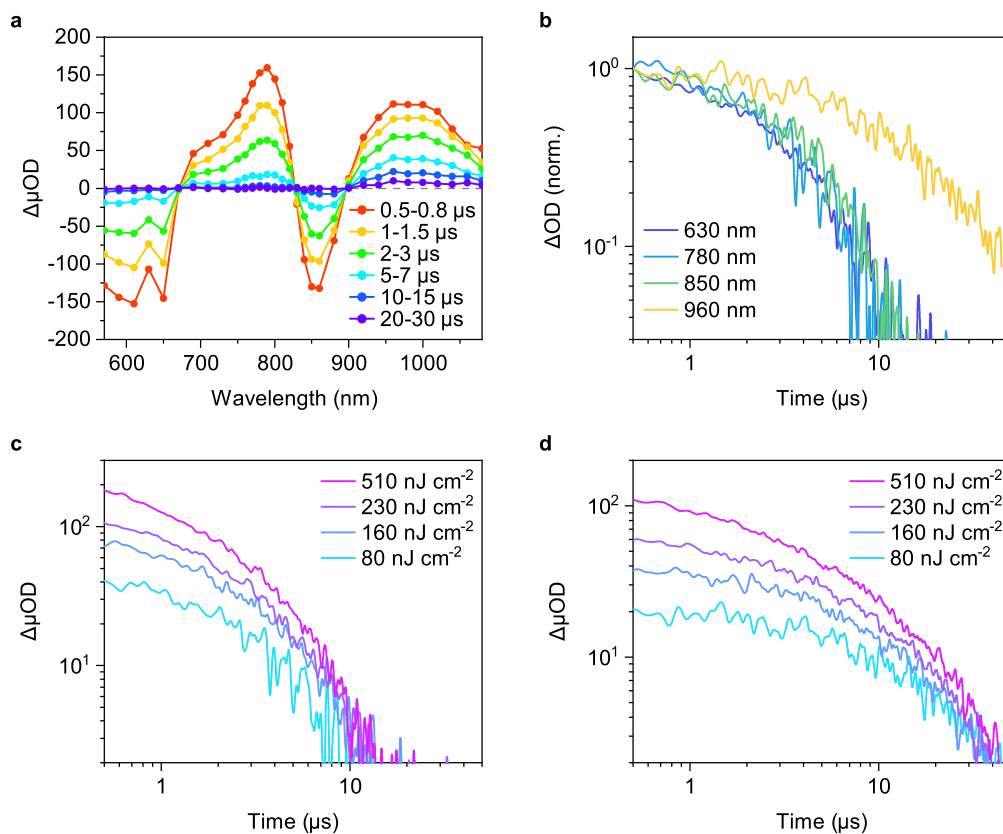


Fig. S14. **a** TA spectra of the PM6/Y6 blend film on the microsecond time scale. The excitation wavelength was 532 nm with a fluence of 510 nJ cm^{-2} . **b** Normalized time evolution of TA signals monitored at four characteristic wavelengths with a fluence of 80 nJ cm^{-2} . **c,d** Excitation-fluence dependence of TA decays monitored at **(c)** 780 nm and **(d)** 960 nm.

Here, we provide some additional evidence for the assignments of TA spectra.

Fig. S15 shows the TA spectra of a PM6/PCBM blend film. The TA spectra of a pristine PM6 film is also shown as a reference (broken line). For the pristine PM6 film, a large PIA band at ~ 1200 nm was observed immediately after photoexcitation, which can be assigned to singlet excitons of PM6.^{S15,S16} The singlet excitons monitored at 1200 nm decayed rapidly in the blend film, whereas a new PIA band at ~ 900 nm was also observed, which is assigned to PM6 hole polarons.^{S15,S16}

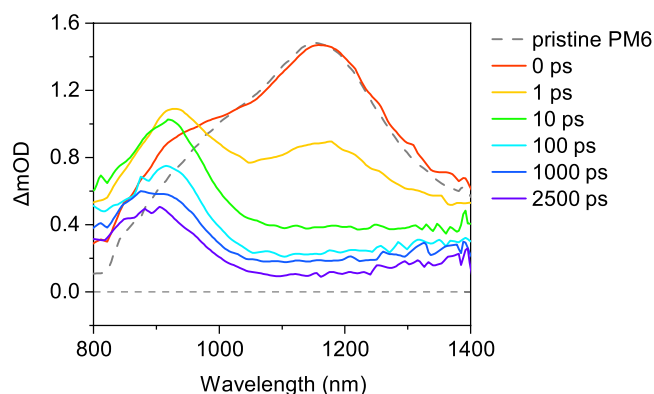


Fig. S15. TA spectra of a PM6/PCBM blend film and a pristine PM6 film as a reference. The excitation wavelength was 590 nm with a fluence of $7.1 \mu\text{J cm}^{-2}$.

Interestingly, the PIA band at ~ 970 nm in the PM6/Y6 blend film extends into the longer wavelength region and approaches ~ 1100 nm, suggesting that the Y6 anion PIA band overlaps in this region. To confirm this, we show the TA spectra of the PTB7-Th/Y6 blend film since PTB7-Th hole polarons do not exhibit strong PIA in the 900–1000 nm region.^{S17} Fig. S16a shows the TA spectra of the PTB7-Th/Y6 blend film excited at 800 nm. Immediately after photoexcitation, Y6 singlet excitons and GSB bands were observed, as in the case of the PM6/Y6 blend film. Then, the hole polarons and GSB of PTB7-Th, peaking at ~ 1150 nm and ~ 730 nm, respectively,^{S17} increased rapidly, indicating hole transfer from Y6 to PTB7-Th. A PIA band similar to that of the PM6/Y6 blend in the 900–1000 nm region decayed together with the PTB7-Th hole polaron on later time scale, indicating that this PIA is attributable to Y6 anion. Therefore, the broad PIA peaking at ~ 970 nm observed in the PM6/Y6 blend film is a superposition of PM6 hole polaron and Y6 anion.

The positive PIA at 780 nm was also observed for the PTB7-Th/Y6 and annealed P3HT/Y6 films all the way from the picosecond time scale to the microsecond time scale, as shown in Figs. S16–S18. The observation of this band in all three blend films (PM6/Y6, PTB7-Th/Y6, and annealed P3HT/Y6) on the microsecond time scale is clear evidence that this band is attributable to Y6 anions. Because this band is not observed in the as-cast P3HT/Y6 blend film, the 780 nm band can be attributable to Y6 anions in the crystalline domains. This assignment is further supported by the bimodal charge decay dynamics observed for the PM6/Y6 blend film, as shown in Fig. S14b. Interestingly, TA signals at 960 nm decay more slowly than those at 780 nm (Fig. S14b). Such bimodal charge-transport behaviour has been observed in other OSCs.^{S18} In line with previous reports, the slow decay at 960 nm is a sign that charges in relatively disordered regions are responsible for the PIA at 960 nm, where charges are trapped at shallow trap sites. Since the decay at 780 nm coincides well with the

GSB signals at 630 and 850 nm, the TA signal at 780 nm is responsible for charge transport, i.e., the 780 nm band can be attributable to Y6 anions in crystalline domains; hence, this band is more important than that at 960 nm in terms of FC generation.

Note that for the PTB7-Th/Y6 blend film the 780 nm band cannot be attributed to the EA of PTB7-Th because it shows a peak wavelength at ~ 740 nm.^{S17} On the other hand, the absorption edge of the PTB7-Th hole polaron is observed at this wavelength, which is the reason for the complex (three exponential function) time evolution of this band for the PTB7-Th/Y6 blend film, as discussed in the next section.

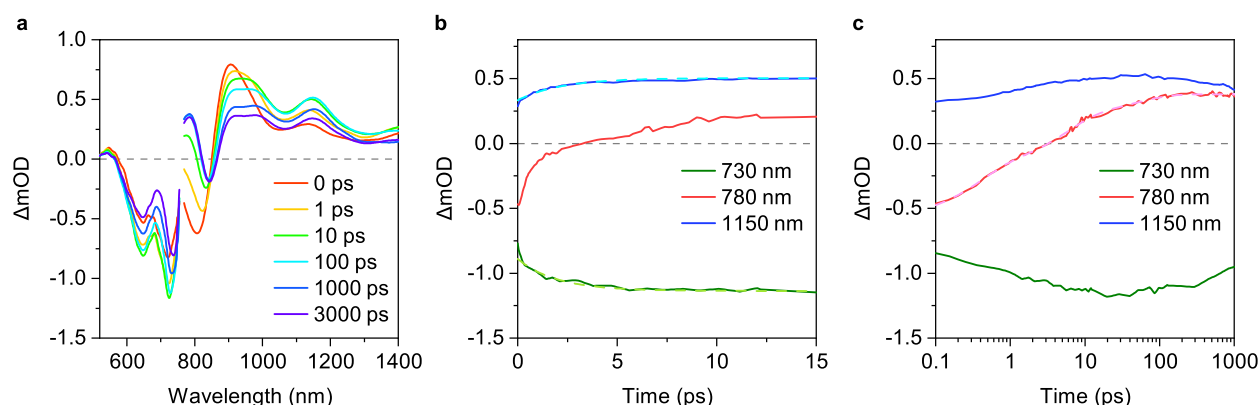


Fig. S16. **a** TA spectra of the PTB7-Th/Y6 blend film. The excitation wavelength was 800 nm with a fluence of $2.4 \mu\text{J cm}^{-2}$. **b** Time evolution of TA signals on an early time scale. Colored broken lines represent the best fit curves by a sum of an exponential function and a constant fraction. **c** Time evolution of TA signals on a later time scale. The coloured broken line represents the best fit curves by a sum of three exponential functions and a constant fraction. Each time constant (fraction) was 0.37 ps (40.5%), 5.4 ps (41.7%), and 51.1 ps (17.8%).

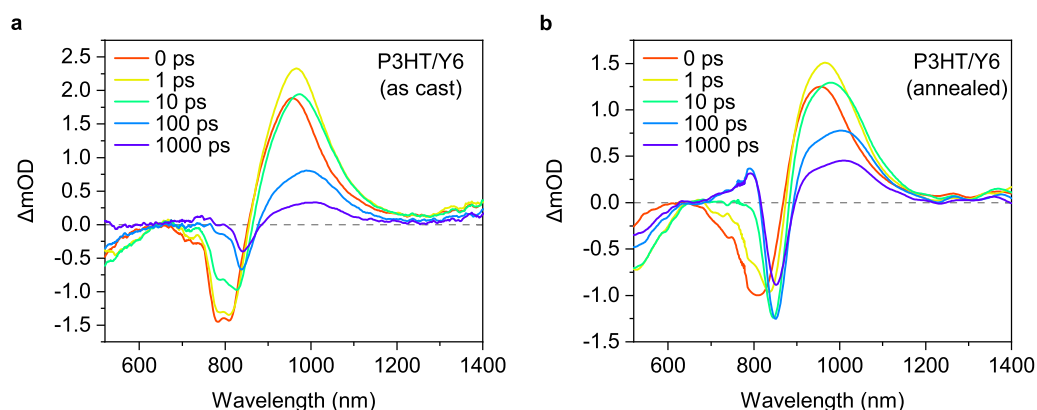


Fig. S17. TA spectra of **(a)** as-cast and **(b)** annealed P3HT/Y6 blend films. The excitation wavelength was 800 nm with a fluence of $5.5 \mu\text{J cm}^{-2}$.

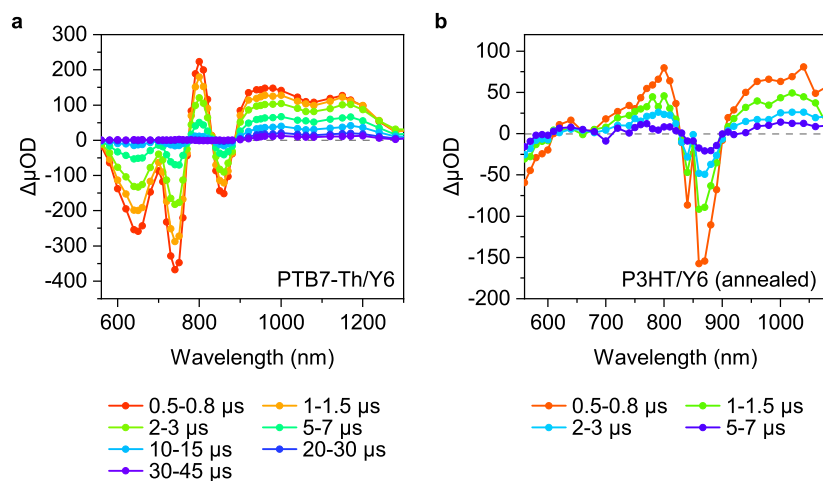


Fig. S18. TA spectra of the (a) PTB7-Th/Y6 and (b) annealed P3HT/Y6 blend films on the microsecond time scale. The excitation wavelength was 532 nm with a fluence of 0.6 and 3.0 $\mu\text{J cm}^{-2}$, respectively.

Time evolution of the TA spectra of the PTB7-Th/Y6 blend film

The time evolution of the TA signals measured at 730 nm (GSB of PTB7-Th) and 1150 nm (hole polaron) were well fitted by the sum of an exponential function and a constant fraction (Fig. S16b). The time constants were found to be ~ 2.0 ps and ~ 2.2 ps for 730 nm and 1150 nm, respectively, indicating that Y6 excitons dissociate into charges on a time scale of ~ 2.0 ps. On the other hand, PIA at 780 nm increased more slowly, again as in the case of the PM6/Y6 blend. This curve was fitted by a sum of three exponential functions and a constant fraction (Fig. S16c). The average time constant was ~ 11.5 ps (each component is described in the figure caption). Thus, this rise is apparently slower than that of exciton dissociation, but considerably faster than the decay of hole polarons (~ 1.8 ns, monitored at 1150 nm). These results again confirm that the ~ 780 nm band emerges independently of exciton dissociation and charge recombination. Rather, it should be attributed to the charge shift from the D/A interface into the bulk of the Y6 domain, as discussed in the main text.

Excitation fluence dependence of exciton decay kinetics

Fig. S19 shows the excitation-fluence dependence of the time evolution on an early time scale monitored at 630 nm (PM6 GSB) and 830 nm (Y6 GSB). As we selectively excite Y6, only hole polarons are responsible for PM6 GSB, and hence PM6 GSB appears only when Y6 excitons dissociate into charges at the D/A interface; thereby, the rise rate of PM6 GSB is exactly the same with the decay rate of Y6 excitons. The rise kinetics of PM6 GSB as well as the decay kinetics of Y6 GSB were independent of the excitation fluence at $<3.5 \mu\text{J cm}^{-2}$, indicating that SSA of Y6 excitons can be ignored in the blend film at low excitation fluences. On the other hand, the rise and decay kinetics become faster with increasing excitation fluence, indicating the contribution of SSA to the deactivation of Y6 singlet excitons.

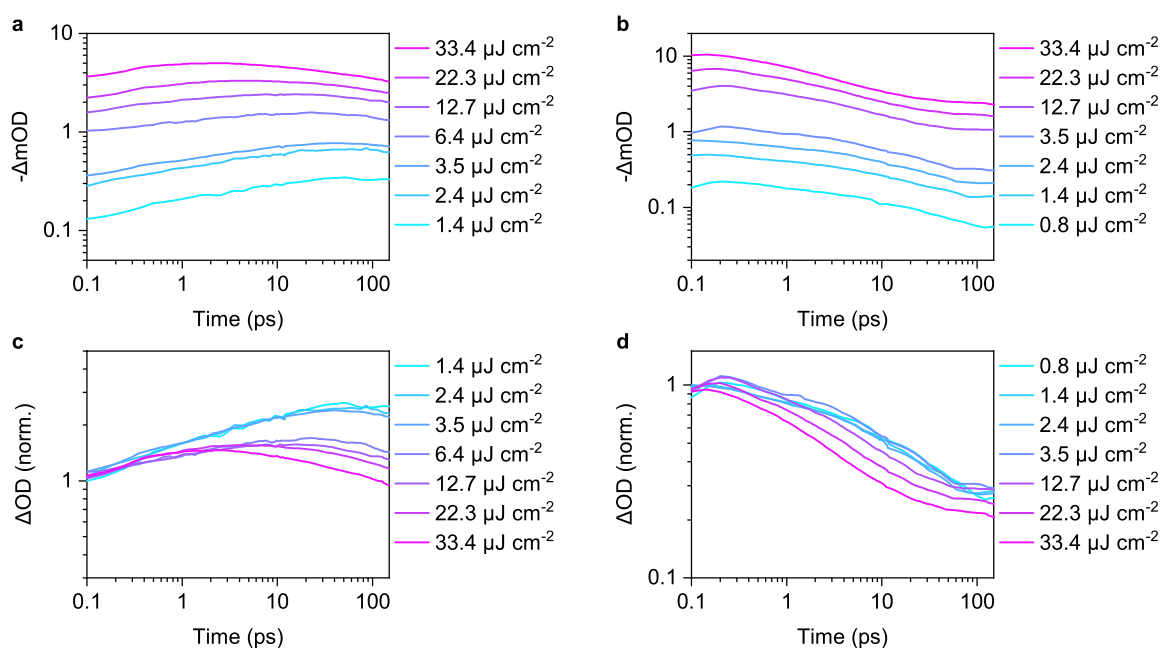


Fig. S19. **a** Rise kinetics of PM6 GSB monitored at 630 nm after photoexcitation at 800 nm. **b** Decay kinetics of Y6 GSB monitored at 830 nm after photoexcitation at 800 nm. **c,d** Normalized rise and decay kinetics of **a** and **b**, respectively.

Charge generation kinetics in the PM6/Y6 blend

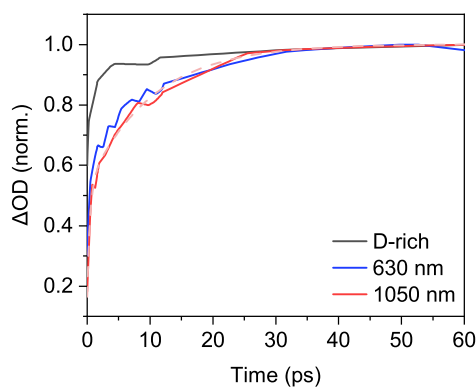


Fig. S20. Normalized time evolution of TA signals for the optimized PM6/Y6 blend film monitored at 630 (blue) and 1050 (red) nm. The excitation wavelength was 800 nm with a fluence of $1.4 \mu\text{J cm}^{-2}$. The rise at 1050 nm was fitted using the sum of two exponential functions with the time constants of 0.4 ps (43%) and 10.2 ps (57%) and a constant fraction (broken line). The grey line shows normalized time evolution of TA signals for the D-rich PM6/Y6 blend film monitored at 970 nm.

TA spectra of the PM6/Y6 blend film after band-edge excitation

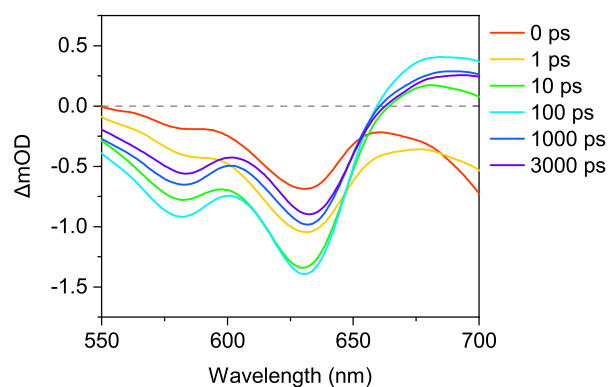


Fig. S21. TA spectra of the PM6/Y6 blend film in the visible region. The excitation wavelength was 900 nm with a fluence of $13.3 \mu\text{J cm}^{-2}$.

Reorganization energy

The reorganization energy was calculated by using model compounds of isolated PM6 dimer and Y6 monomer, wherein alkyl side chains were shortened to reduce the computational effort, as shown in Fig. S22. The total reorganization energy λ (Fig. S23) was calculated to be ~ 0.27 eV, of which ~ 0.19 eV was derived from PM6 and ~ 0.08 eV from Y6. The smaller λ of Y6 is consistent with its relatively high crystallinity.

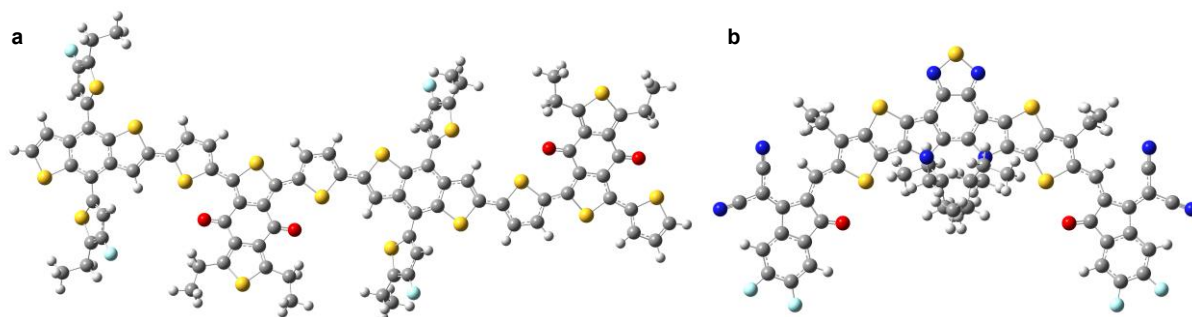


Fig. S22. Optimized structures of model compounds in the charged state obtained by the DFT calculations; **a** PM6 dimer, and **b** Y6.

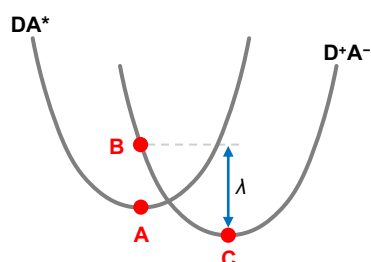


Fig. S23. Schematic defining the reorganization energy λ , which was calculated as the difference in total energies at the points **B** and **C**. The total energy at the point **B** was calculated as a sum of the total energies obtained by single point calculations of PM6 dimer and Y6 in the charged states using the geometry at the point **A**, where PM6 dimer was optimized in the ground state, whereas Y6 in the singlet excited state. The total energy at the point **C** was calculated as a sum of the total energies of the optimized PM6 dimer and Y6 in the charged states.

Late emergence of the 760 nm signal in the PM6/Y6 blend film

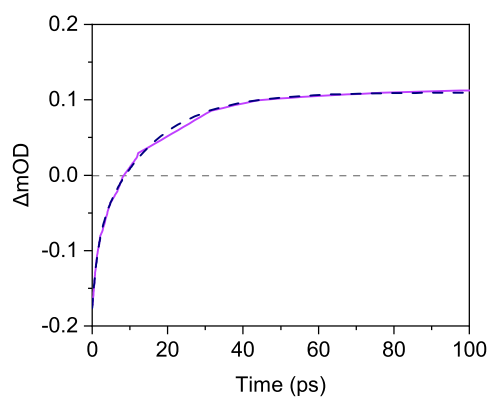


Fig. S24. Time evolution of TA signals for the optimized PM6/Y6 blend film monitored at 760 nm. The excitation wavelength was 800 nm with a fluence of $1.4 \mu\text{J cm}^{-2}$. The rise kinetics at 760 nm was fitted using the sum of two exponential functions with the time constants of 1.5 ps (31%) and 14.8 ps (69%) and a constant fraction (blue broken line).

Supplementary comment on the Y6 GSB peak shift

Here, we provide an additional explanation for the Y6 GSB shift. As the density of states (DOS) of organic semiconductors in the solid state is widely distributed in energy, charges generated at the D/A interface are relaxed to the lower energy sites, that is, downhill energy relaxation. We consider the absorption spectrum of the molecule occupied by the charge at each time. As the steady-state absorption spectrum of Y6 is redshifted with increasing crystallinity (Fig. S4), the absorption spectrum of the molecule occupied by the charge is redshifted during downhill relaxation. Since the GSB signal is caused by a decrease in the steady-state absorption owing to excitation of the molecule, the GSB signal reflects where the transient species resides at each time. Therefore, we conclude in the main text that the GSB redshift can be rationalized by downhill relaxation.

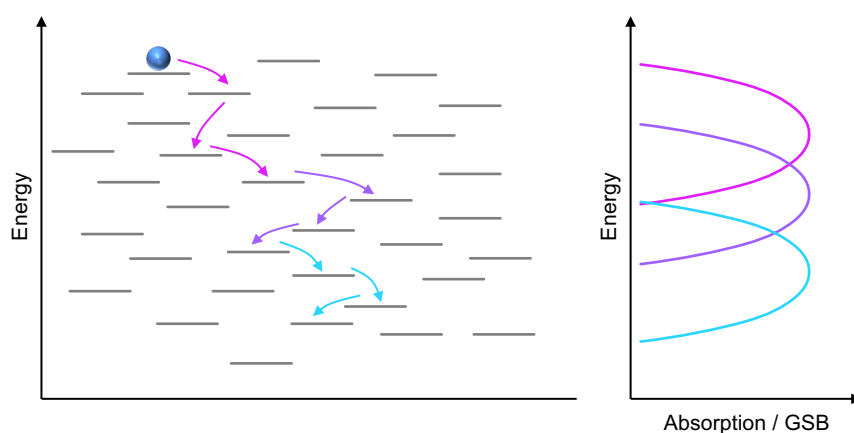


Fig. S25. Schematic showing downhill energy relaxation of charges in DOS and the corresponding absorption/GSB spectra.

Time evolution of EA

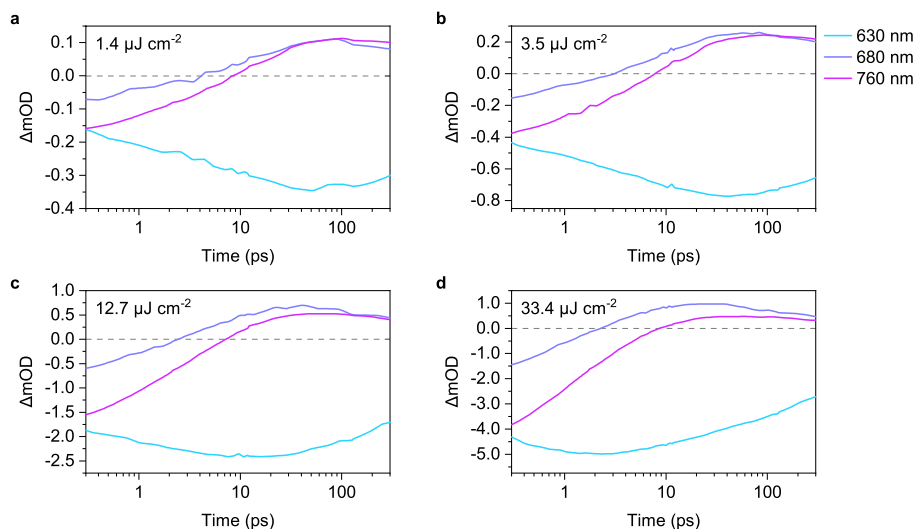


Fig. S26. Time evolutions of TA signals after photoexcitation at 800 nm with various excitation fluences.

Normalized time evolution of EA

The TA signals in Fig. S26 are normalized to clarify the differences in peak positions, as follows. First, the TA signal at 0.1 ps was subtracted from the entire signal. Then, the remaining signal was divided by its largest absolute value to provide values in the 0–1 range (Fig. S27). It should be emphasized that the above data processing does not change the time at which the TA signal approaches the maximum (absolute) value. In other words, the fact that the (absolute) maximum values of the EA signals were observed slightly after the hole transfer is independent of how these data are normalized.

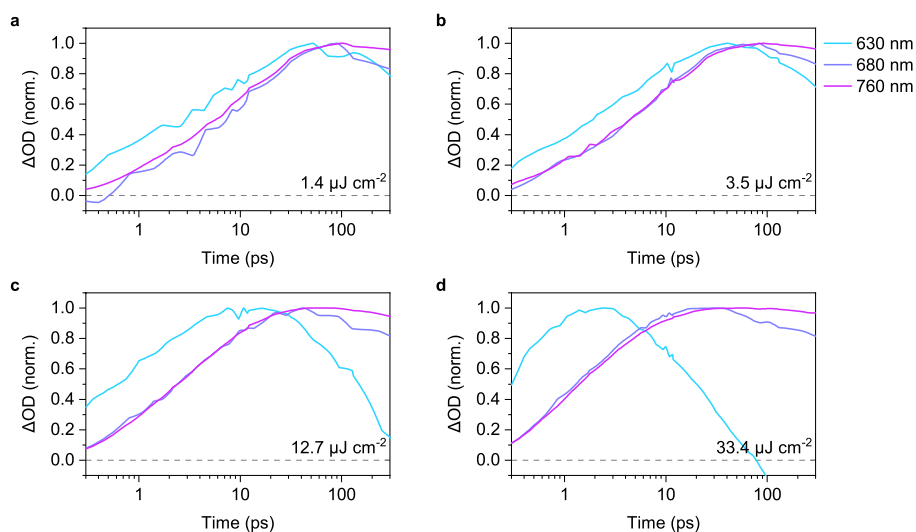


Fig. S27. Normalized time evolutions of TA signals after photoexcitation at 800 nm with various excitation fluences.

Difference in the time evolution of charge TA and EA signals

When an exciton dissociates to form an electron-hole pair at the D/A interface, the electron-hole pair generates a dipole-like local electric field. Surrounding molecules in the ground state are therefore perturbed by the local electric field, resulting in a Stark shift in the steady-state absorption spectrum. The pump-probe TA spectroscopy monitoring of the intensity difference between the transmitted probe pulse with and without pump pulse is equivalent to monitoring the intensity difference between the transmitted probe pulse with and without the local electric field. As a result, a transient EA spectrum is necessarily included in the TA spectrum.

Fig. S28 is a schematic showing the difference in the time evolution of charge TA and transient EA signals. The signal amplitude of the charge TA remains unchanged during charge dissociation process as it is a function of the charge density. In contrast, because that of the transient EA signal is a function of both the charge density and the separation distance between the electron and hole, it increases with increasing the separation distance. Therefore, the fact that the EA signals reached their maximum value slightly after the occurrence of hole transfer, as shown in Fig. 5b, indicates that long-range spatial dissociation of CT states takes place on a time scale of picoseconds.

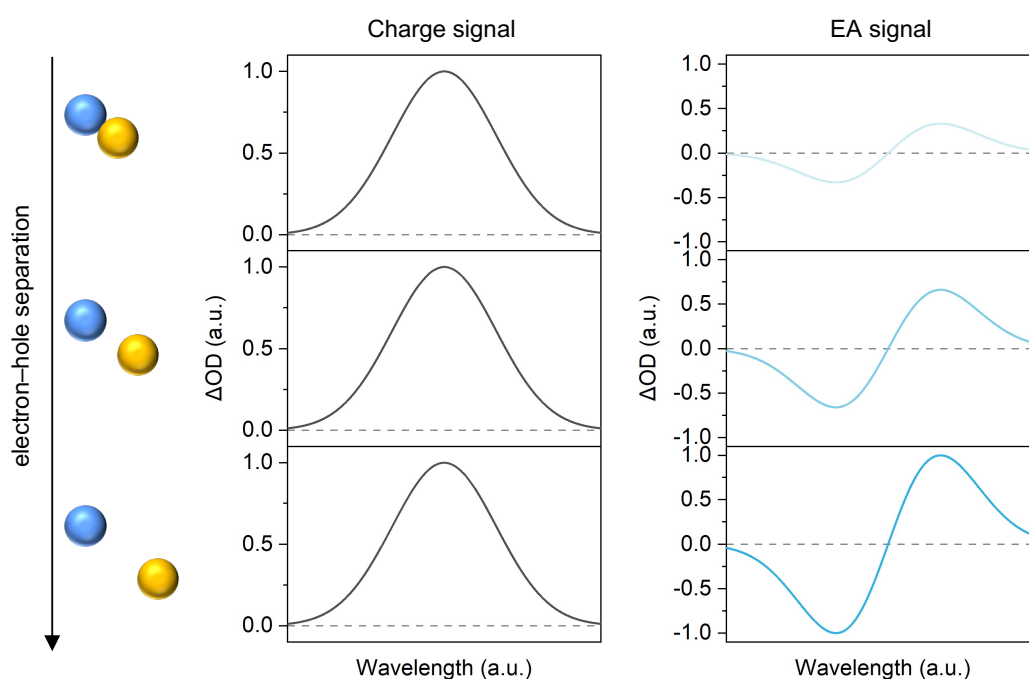


Fig. S28. Schematic showing the difference in the time evolution of charge TA and EA signals.

TA spectra of the PM6/Y6 blend film after polymer selective excitation

Fig. S29a shows the TA spectra of the PM6/Y6 blend film excited at 600 nm. The singlet excitons of PM6 observed at 1200 nm decayed very rapidly, accompanied by an increase in Y6 GSB. As shown in Fig. S29b, the time constant of the decay (rise) was found to be ~ 0.6 ps (~ 0.5 ps), indicating fast electron transfer from PM6 to Y6.

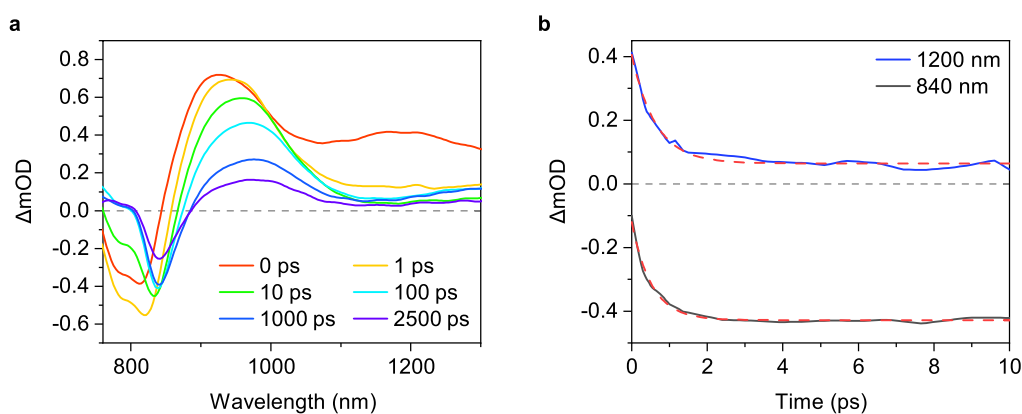


Fig. S29. **a** TA spectra of the PM6/Y6 blend film. The excitation wavelength was 600 nm with a fluence of $5.0 \mu\text{J cm}^{-2}$. **b** Time evolutions of PM6 singlet excitons at 1200 nm (blue) and Y6 GSB at 840 nm (black). The red broken lines are the best fits by a sum of an exponential function and a constant fraction.

Excitation fluence dependence of charge decay kinetics

Fig. S30 shows the excitation-fluence dependence of the decay kinetics of Y6 GSB monitored at 850 nm on a later time scale. GSB signals recovered faster with increasing excitation fluence even under low excitation fluences, suggesting that the FC generation is efficient and hence, bimolecular charge recombination is the dominant decay channel for the PM6/Y6 blend film.

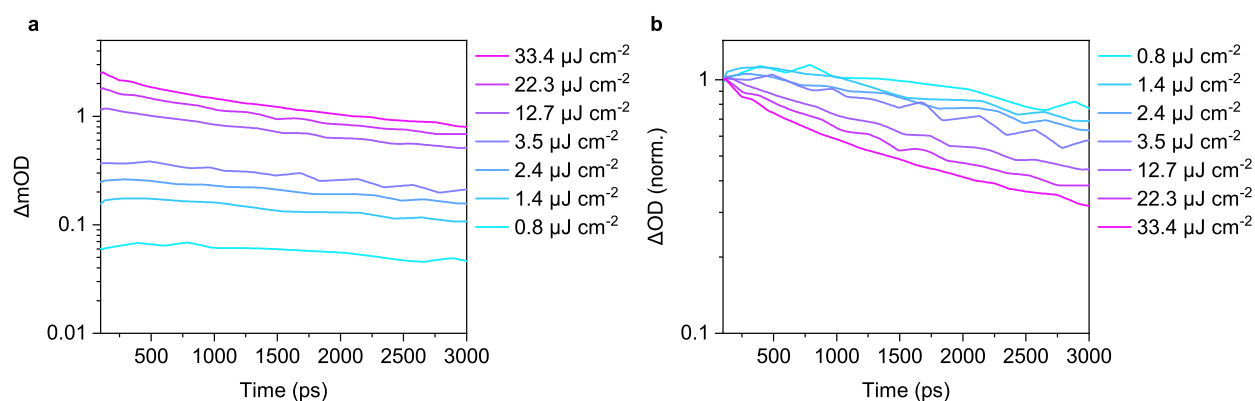


Fig. S30. **a** Decay kinetics of Y6 GSB monitored at 850 nm after photoexcitation at 800 nm. **b** Normalized kinetics of **a**.

Temperature dependence of the PM6/Y6 blend

The TA signals at 780 nm increased with decreasing temperature because the GSB band red-shifted with decreasing temperature (Fig. S32a), thereby mitigating the spectral overlap between the positive PIA and the GSB. It should be noted that this complicated temperature dependence at 780 nm does not affect our conclusion.

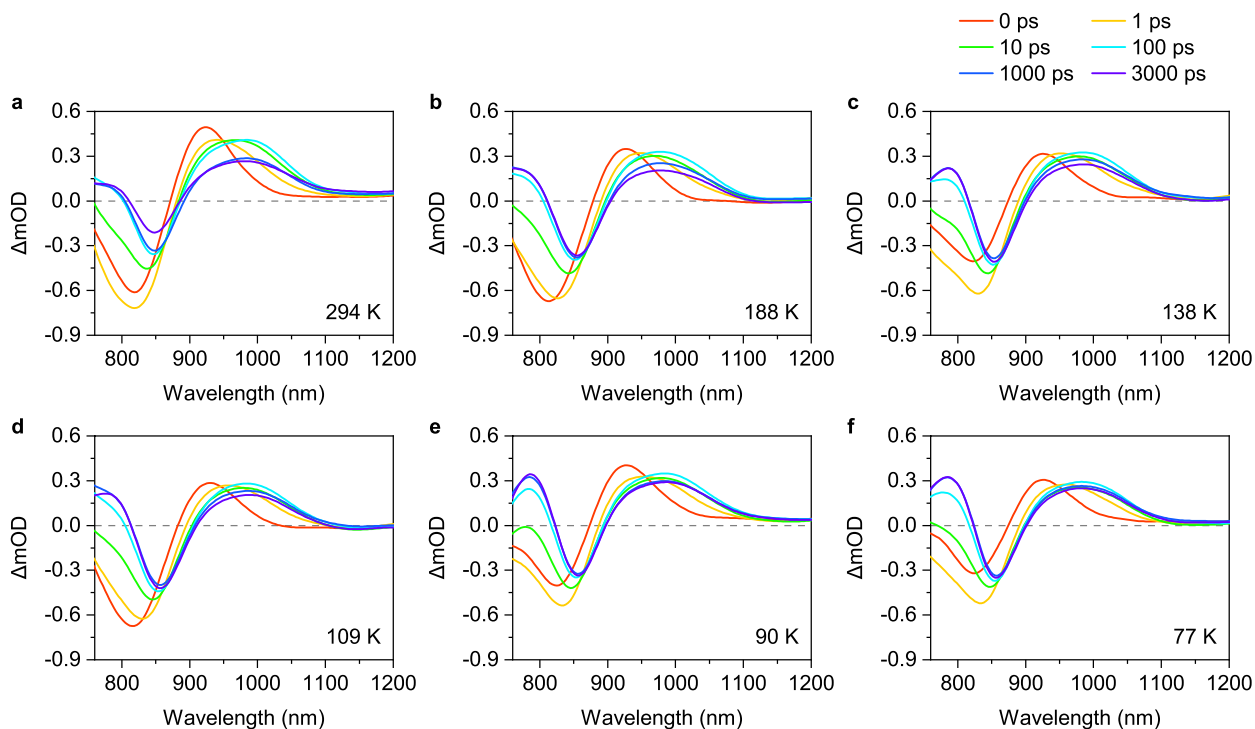


Fig. S31. TA spectra of the PM6/Y6 blend film measured at various temperatures.

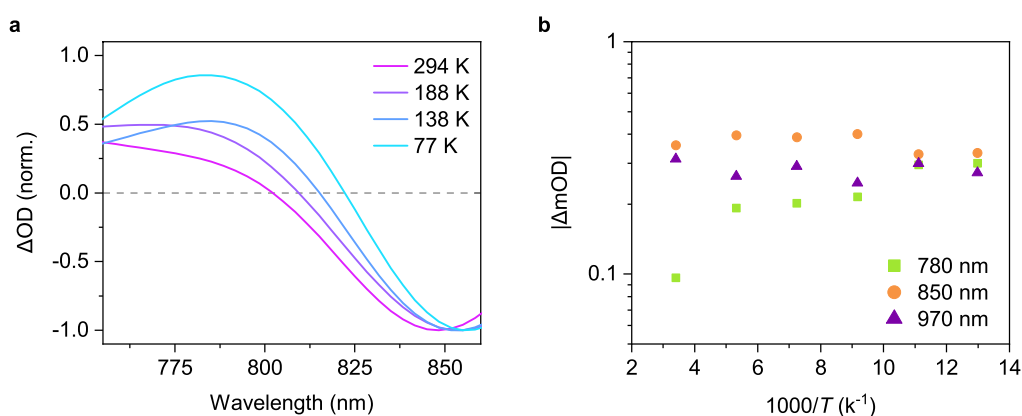


Fig. S32. **a** Normalized TA spectra of the PM6/Y6 blend film at 500 ps after photoexcitation measured at various temperatures. **b** Arrhenius plot for the TA amplitude.

Fig. S33 shows the Arrhenius plot for the inverse of the rise time constant k_{rise} monitored at 780 nm (same as Fig. 7c). The red line shows the best fit curve with the following Arrhenius equation using four data points on the left side

$$k_{\text{rise}} = A \exp\left(-\frac{E_a}{k_B T}\right) \quad (\text{S2})$$

where E_a is the activation energy. E_a was determined to be ~ 9.4 meV, which is the upper limit of the estimation. On the other hand, we obtained the green curve with E_a of ~ 4.0 meV when all data points were used for the fitting.

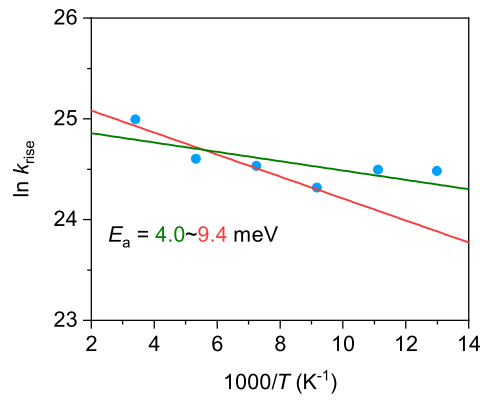


Fig. S33. Arrhenius plot for the inverse of the rise time constant k_{rise} monitored at 780 nm. The solid lines represent the best fit curves with Equation S2.

Triplet generation via bimolecular charge recombination

Fig. S34a shows the TA spectra of the PM6/Y6 blend film at a high excitation fluence. A long-lived PIA is pronounced at ~ 1400 nm at later times (Fig. S34b), which is attributable to Y6 triplet excitons generated through bimolecular charge recombination.^{S6,S7}

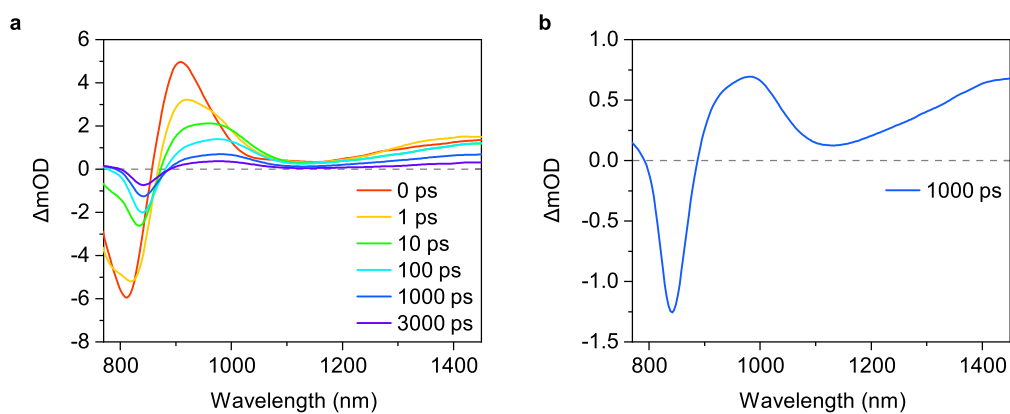


Fig. S34. **a** TA spectra of the PM6/Y6 blend film. The excitation wavelength was 800 nm with a fluence of $22.3 \mu\text{J cm}^{-2}$. **b** Enlarged TA spectra at 1000 ps.

TA data processing via total variation regularization

Herein, we introduce a new denoising method for time-resolved spectroscopy based on the total variation (TV) regularization. The original TV regularization method was introduced in the context of digital image restoration under Gaussian noise^{S19} and has now evolved into a more general technique for solving inverse problems.

In this method, we assume that the degradation of the observed TA data $\mathbf{v} \in \mathbb{R}^{m \times n}$ can be modeled as

$$\mathbf{v} = \bar{\mathbf{u}} + \mathbf{n} \quad (\text{S3})$$

where $\bar{\mathbf{u}} \in \mathbb{R}^{m \times n}$ is an unknown original noise-free signal, and $\mathbf{n} \in \mathbb{R}^{m \times n}$ is an additive noise. Owing to the continuity of both the absorption spectra of organic molecules and their decay kinetics, we can assume that $\bar{\mathbf{u}}$ is piecewise smooth, i.e. the second derivative of $\bar{\mathbf{u}}$ is sparse.

By letting $\mathbf{D}_x, \mathbf{D}_y \in \mathbb{R}^{m \times m}$ be the vertical and horizontal discrete gradient operators, respectively, with the Newmann boundary, the TV of the second order for each direction of the TA data matrix is given as

$$\text{TV}_{x,y}(\mathbf{u}) := \mathbf{D}_{x,y}^2 \mathbf{u} \quad (\text{S4})$$

For example

$$\mathbf{D}_x := \begin{pmatrix} -1 & 1 & 0 & 0 & \cdots & 0 \\ 0 & -1 & 1 & 0 & \cdots & 0 \\ \vdots & & \ddots & \ddots & & \vdots \\ 0 & \cdots & 0 & -1 & 1 & 0 \\ 0 & \cdots & 0 & 0 & -1 & 1 \\ 0 & \cdots & 0 & 0 & 0 & 0 \end{pmatrix} \quad (\text{S5})$$

Therefore, to obtain $\bar{\mathbf{u}}$, the following convex optimization problem should be solved:

$$\min_{\mathbf{u} \in \mathbb{R}^{m \times n}} \lambda_1 \|\text{TV}_x(\mathbf{u})\|_p + \lambda_2 \|\text{TV}_y(\mathbf{u})\|_p \quad \text{s.t. } \mathbf{u} \in B_\varepsilon \quad (\text{S6})$$

where

$$B_\varepsilon := \|\mathbf{v} - \mathbf{u}\|_2 \leq \varepsilon \quad (\text{S7})$$

The set B_ε is a \mathbf{v} -centred l_2 -norm ball with a radius ε , which serves as a fidelity constraint with respect to the observation \mathbf{v} . Prefactors λ_1 and λ_2 determine the balance between the vertical and horizontal TV terms, respectively, and $\|\cdot\|_p$ ($p = 1$ or 2) stands for the l_1 - and l_2 -norm, i.e. the sum of absolute values of all the entries of $(*)$ and the Euclidean norm, respectively.

To solve Equation S6, we used a primal-dual splitting method,^{S20,S21} which can solve optimization problems of the form:

$$\underset{\mathbf{x} \in \mathbb{R}^{m \times n}}{\text{argmin}} f(\mathbf{x}) + g(\mathbf{x}) + h(\mathbf{L}\mathbf{x}) \quad (\text{S8})$$

where f is a differentiable convex function with the β -Lipschitzian gradient ∇f for some $\beta > 0$, g and h are proximal functions, and \mathbf{L} is a matrix. The algorithm is given by

$$\mathbf{x}^{(n+1)} = \text{prox}_{\gamma_1 g}[\mathbf{x}^{(n)} - \gamma_1 (\nabla f(\mathbf{x}^{(n)}) + \mathbf{L}^*)] \quad (\text{S9})$$

$$\mathbf{y}^{(n+1)} = \text{prox}_{\gamma_2 h^*}[\mathbf{y}^{(n)} + \gamma_2 \mathbf{L}(2\mathbf{x}^{(n+1)} - \mathbf{x}^{(n)})] \quad (\text{S10})$$

where prox denotes the proximity operator, h^* is the Fenchel-Rockafellar conjugate function^{S22} of h , and \mathbf{L}^* is the adjoint operator of \mathbf{L} . In addition, γ_1 and γ_2 ($\gamma_1, \gamma_2 > 0$) are the step sizes that satisfy $\gamma_1^{-1} - \gamma_2 \lambda_1(\mathbf{L}^* \mathbf{L}) \geq \beta/2$, where $\lambda_1(*)$ stands for the maximum eigenvalue of $*$. Under some mild conditions of g , h , and \mathbf{L} , the sequence converges to a solution for Equation S8.

Here, we demonstrate TV denoising for TA spectroscopy. Fig. S35a shows the TA data of the PM6/Y6 blend film measured under a high excitation fluence of $50 \mu\text{J cm}^{-2}$. Owing to the high excitation fluence, the SNR of the data was reasonably high without any denoising methods. Therefore, we used these data as a “known” $\bar{\mathbf{u}}$. Then, we added Gaussian noise to artificially degrade the data (Fig. S35b).

Before applying TV denoising, we performed a normal moving average method for the degraded data (Figs. S35c,d). Denoised data labeled “movave 1” and “movave 2” represent the data obtained by the moving average method, wherein the i,j -th data are replaced by an average over between the $i \pm 2, j \pm 2$ -th, and $i \pm 5, j \pm 5$ -th data, respectively (i.e. the window size of “movave 1” and “movave 2” are 5 and 11, respectively). The residue of the Gaussian noise was observed when the window size of the moving average was 5 (“movave 1”, Figs. S35c and S37a, blue line). On the other hand, although the residue was mitigated when the window size was 11 (“movave 2”, Figs. S35d and S37a, green line), the edge feature around the time origin is lost for “movave 2” (Fig. S37c, green line). For a more quantitative discussion, we evaluated the root mean squared error (RMSE) between the original and noisy/denoised data. As shown in Fig. S36a, the RMSE of the “movave 1” and “movave 2” data were ~ 4.9 and ~ 8.3 times smaller than that of the artificially degraded data, respectively. We also evaluated the slope at the time origin and compared to that of the original data. The relative slope obtained by a linear fit to the onset around the time origin decreased to ~ 0.64 and ~ 0.42 , respectively, for the “movave 1” and “movave 2” data, meaning that the apparent time resolution of the TA data degrades with increasing the window size. These results indicate that it is difficult to simultaneously remove noise and retain edges using the moving average method.

Figs. S35e–g show data denoised using the TV regularization method with different p values (details can be found in the caption of Fig. S35). We found that all TV data with different p values exhibited a lower RMSE and a better apparent time resolution than those obtained using the moving average method (Fig. S36). We obtained the best solution by the TV regularization method with $p = 2$ (l_2 -norm) for the vertical (spectrum) direction and $p = 1$ (l_1 -norm) for the horizontal (kinetics) direction, as shown in Figs. S36 and S37. The RMSE

is ~ 9.9 times smaller than that of the artificially degraded data, although the relative slope at the onset remained as large as ~ 0.88 . Notably, the TV regularization method demonstrated here is also advantageous for maintaining the wavelength resolution for the same reasons. We could obtain denoised TA kinetics data if the TA data were averaged over the vertical direction. However, this is equivalent to degrading the apparent wavelength resolution of the TA data, which is undesirable when the TA data consist of a superposition of various transient species. In contrast, the TV regularization method maintains the apparent wavelength resolution.

It should be emphasized that this method is effective for any kind of time-resolved spectroscopic techniques such as time-resolved PL, THz, microwave conductivity measurements. In summary, TV regularization method demonstrated here is a highly effective denoising method for time-resolved spectroscopic techniques.

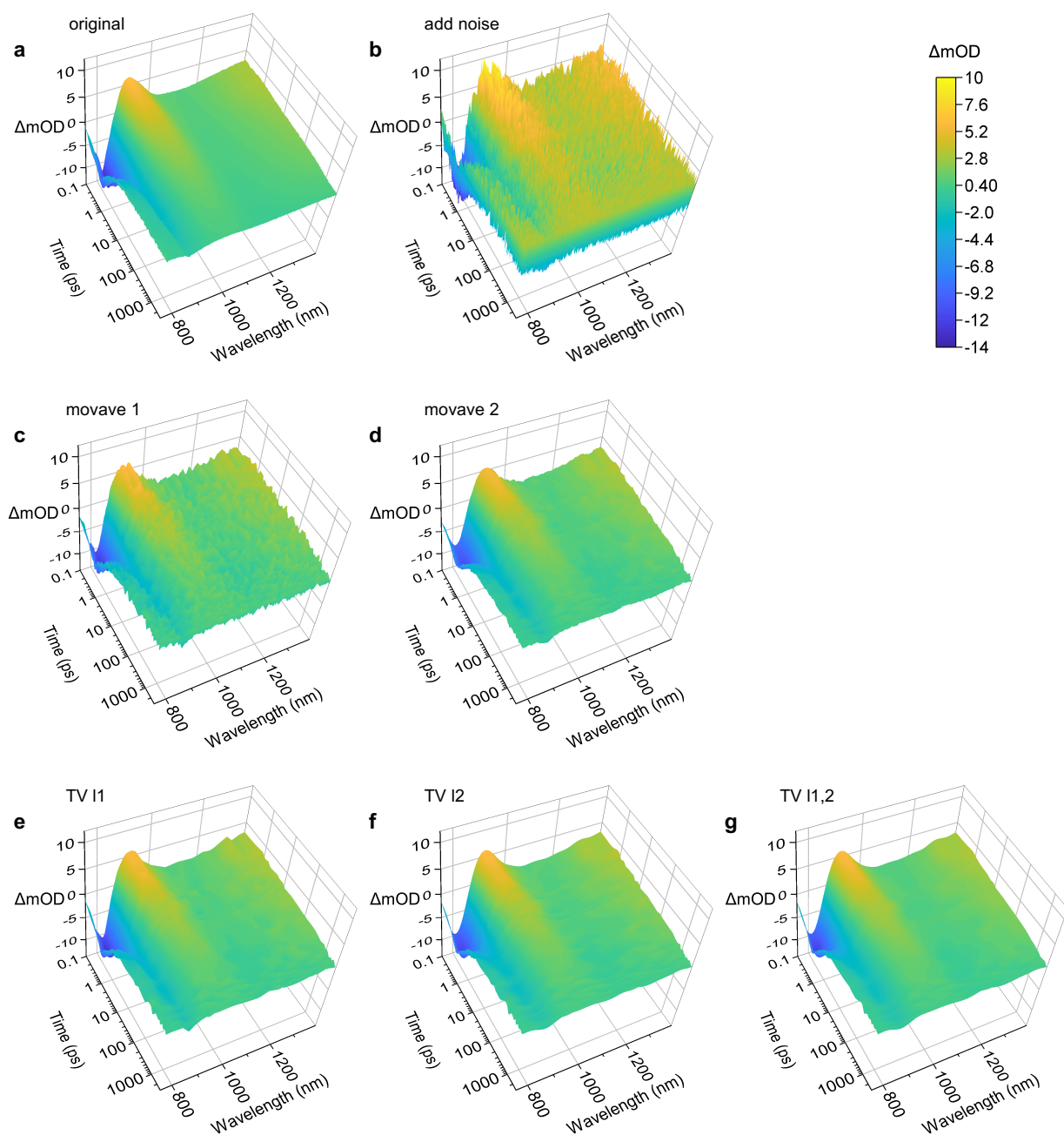


Fig. S35. Surface plot of various datasets. Original: original TA data; add noise: artificially degraded data by adding a Gaussian noise; movave 1,2: denoised data by the moving average method with different window sizes (window size: “movave 1” = 5, “movave 2” = 11); TV l1 and TV l2: data denoised using by the TV regularization method with $p = 1$ (l_1 -norm) and 2 (l_2 -norm), respectively; TV l1,2: data denoised using the TV regularization method with $p = 2$ (l_2 -norm) for the vertical direction and $p = 1$ (l_1 -norm) for the horizontal direction.

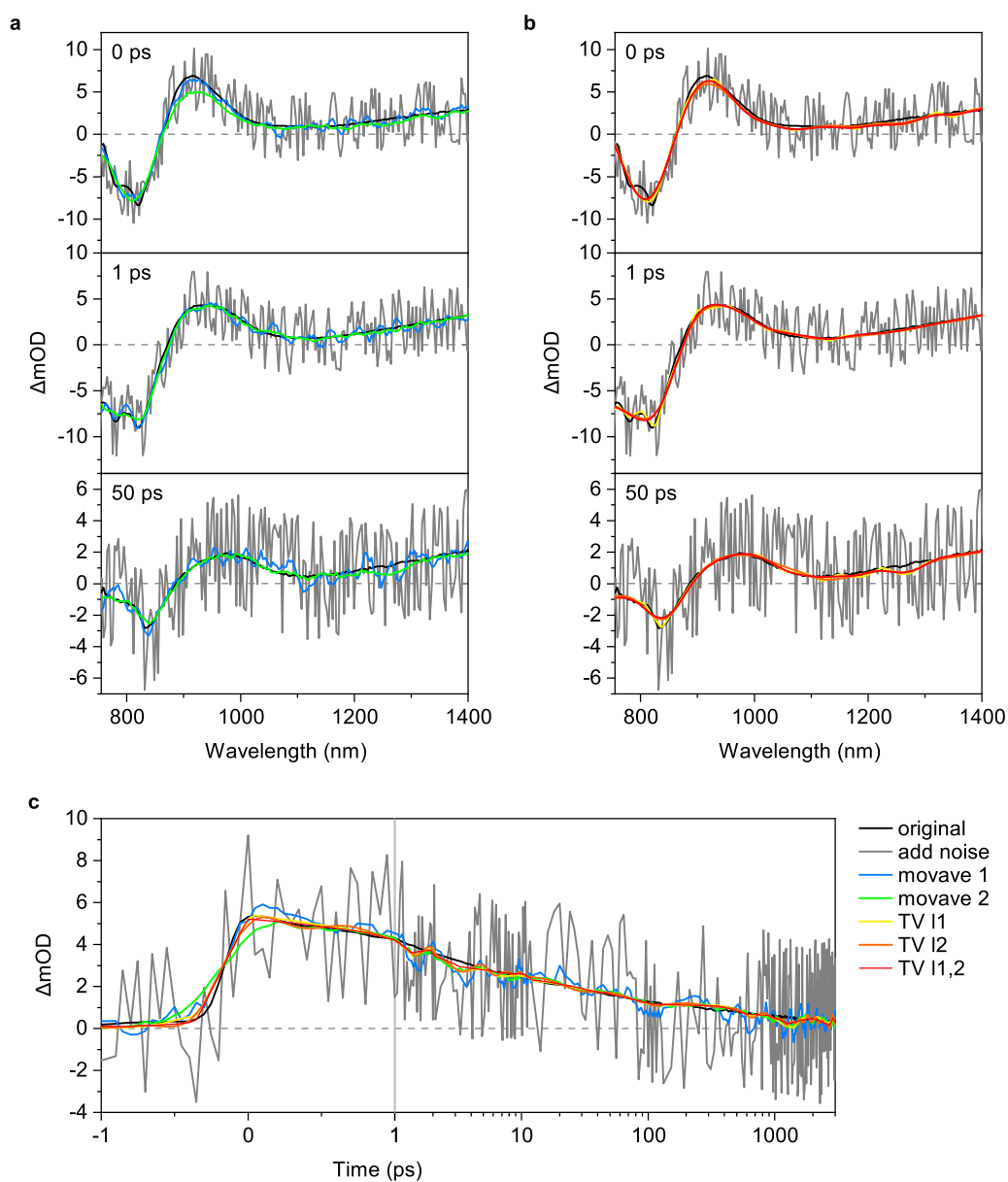
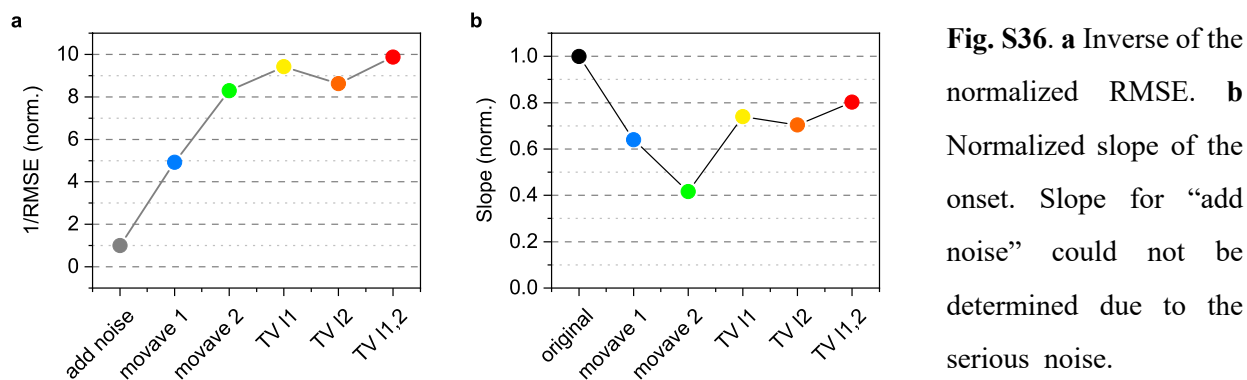


Fig. S37. a TA spectra denoised by the moving average method. **b** TA spectra denoised by the TV regularization method. **c** Time profiles obtained by various denoising methods.

References

- S1. H. Ohkita, Y. Tamai, H. Benten, S. Ito, *IEEE J. Sel. Top. Quantum Electron.* 2016, **22**, 100-111.
- S2. M. J. Frisch, G. W. Trucks, H. B. Schlegel, G. E. Scuseria, M. A. Robb, J. R. Cheeseman, G. Scalmani, V. Barone, G. A. Petersson, H. Nakatsuji, X. Li, M. Caricato, A. V. Marenich, J. Bloino, B. G. Janesko, R. Gomperts, B. Mennucci, H. P. Hratchian, J. V. Ortiz, A. F. Izmaylov, J. L. Sonnenberg, Williams, F. Ding, F. Lipparini, F. Egidi, J. Goings, B. Peng, A. Petrone, T. Henderson, D. Ranasinghe, V. G. Zakrzewski, J. Gao, N. Rega, G. Zheng, W. Liang, M. Hada, M. Ehara, K. Toyota, R. Fukuda, J. Hasegawa, M. Ishida, T. Nakajima, Y. Honda, O. Kitao, H. Nakai, T. Vreve, K. Throssell, J. A. Montgomery Jr., J. E. Peralta, F. Ogliaro, M. J. Bearpark, J. J. Heyd, E. N. Brothers, K. N. Kudin, V. N. Staroverov, T. A. Keith, R. Kobayashi, J. Normand, K. Raghavachari, A. P. Rendell, J. C. Burant, S. S. Iyengar, J. Tomasi, M. Cossi, J. M. Millam, M. Klene, C. Adamo, R. Cammi, J. W. Ochterski, R. L. Martin, K. Morokuma, O. Farkas, J. B. Foresman and D. J. Fox, *Gaussian 16 Rev. A.01*, Wallingford, CT, 2016.
- S3. K. Jiang, Q. Wei, J. Y. L. Lai, Z. Peng, H. K. Kim, J. Yuan, L. Ye, H. Ade, Y. Zou and H. Yan, *Joule*, 2019, **3**, 3020-3033.
- S4. A. Karki, J. Vollbrecht, A. J. Gillett, S. S. Xiao, Y. Yang, Z. Peng, N. Schopp, A. L. Dixon, S. Yoon, M. Schrock, H. Ade, G. N. M. Reddy, R. H. Friend and T.-Q. Nguyen, *Energy Environ. Sci.*, 2020, **13**, 3679-3692.
- S5. L. Xu, W. Tao, H. Liu, J. Ning, M. Huang, B. Zhao, X. Lu and S. Tan, *J. Mater. Chem. A*, 2021, **9**, 11734-11740.
- S6. S. Natsuda, Y. Sakamoto, T. Takeyama, R. Shirouchi, T. Saito, Y. Tamai, H. Ohkita, *J. Chem. Phys. C*, 2021, **125**, 20806-20813.
- S7. A. J. Gillett, A. Privitera, R. Dilmurat, A. Karki, D. Qian, A. Pershin, G. Londi, W. K. Myers, J. Lee, J. Yuan, S.-J. Ko, M. K. Riede, F. Gao, G. C. Bazan, A. Rao, T.-Q. Nguyen, D. Beljonne, R. H. Friend, *Nature*, 2021, **597**, 666-671.
- S8. L. Perdigón-Toro, L. Q. Phuong, S. Zeiske, K. Vandewal, A. Armin, S. Shoaee, D. Neher, *ACS Energy Lett.*, 2021, **6**, 557-564.
- S9. K. Vandewal, K. Tvingstedt, A. Gadisa, O. Inganäs and J. V. Manca, *Phys. Rev. B*, 2010, **81**, 125204.
- S10. K. Vandewal, K. Tvingstedt, J. V. Manca and O. Inganäs, *IEEE J. Sel. Top. Quantum Electron.*, 2010, **16**, 1676-1684.
- S11. P. Wan, X. Chen, Q. Liu, S. Mahadevan, M. Guo, J. Qiu, X. Sun, S.-W. Tsang, M. Zhang, Y. Li, S. Chen, *J. Phys. Chem. Lett.*, 2021, **12**, 10595-10602.
- S12. J. Yuan, Y. Q. Zhang, L. Y. Zhou, G. C. Zhang, H. L. Yip, T. K. Lau, X. H. Lu, C. Zhu, H. J. Peng, P. A. Johnson, M. Leclerc, Y. Cao, J. Ulanski, Y. F. Li and Y. P. Zou, *Joule*, 2019, **3**, 1140-1151.

- S13. C. M. Cardona, W. Li, A. E. Kaifer, D. Stockdale, G. C. Bazan, *Adv. Mater.*, 2011, **23**, 2367-2371.
- S14. S. Karuthedath, J. Gorenflot, Y. Firdaus, N. Chaturvedi, C. S. P. De Castro, G. T. Harrison, J. I. Khan, A. Markina, A. H. Balawi, T. A. D. Peña, W. Liu, R.-Z. Liang, A. Sharma, S. H. K. Paleti, W. Zhang, Y. Lin, E. Alarousu, D. H. Anjum, P. M. Beaujuge, S. De Wolf, I. McCulloch, T. D. Anthopoulos, D. Baran, D. Andrienko and F. Laquai, *Nat. Mater.*, 2021, **20**, 378-384.
- S15. T. Umeyama, K. Igarashi, D. Sasada, Y. Tamai, K. Ishida, T. Koganezawa, S. Ohtani, K. Tanaka, H. Ohkita and H. Imahori, *Chem. Sci.*, 2020, **11**, 3250-3257.
- S16. T. Umeyama, K. Igarashi, Y. Tamai, T. Wada, T. Takeyama, D. Sasada, K. Ishida, T. Koganezawa, S. Ohtani, K. Tanaka, H. Ohkita and H. Imahori, *Sustain. Energy Fuels*, 2021, **5**, 2028-2035.
- S17. Y. Tamai, Y. Fan, V. O. Kim, K. Ziabrev, A. Rao, S. Barlow, S. R. Marder, R. H. Friend and S. M. Menke, *ACS Nano*, 2017, **11**, 12473-12481.
- S18. J. Guo, H. Ohkita, S. Yokoya, H. Benten and S. Ito, *J. Am. Chem. Soc.*, 2010, **132**, 9631-9637.
- S19. L. I. Rudin, S. Osher and E. Fatemi, *Physica D*, 1992, **60**, 259.
- S20. L. Condat, *J. Optim. Theory Appl.*, 2013, **158**, 460-479.
- S21. B. C. Vũ, *Adv. Comput. Math.*, 2013, **38**, 667-681.
- S22. S. K. Narang and A. Ortega, *IEEE Trans. Signal Process.*, 2013, **61**, 4673-4685.